2D MXenes with antiviral and immunomodulatory properties: a pilot study against SARS-CoV-2

Mehmet Altay Unal[1#], Fatma Bayrakdar[2#], Laura Fusco[3,4#], Omur Besbinar[1,5], Christopher E. Shuck[6], Süleyman Yalcin[2], Mine Turktas Erken[7], Aykut Ozkul[8], Cansu Gurcan[1,5], Oguzhan Panatli[5], Gokce Yagmur Summak[1], Cemile Gokce[5], Marco Orecchioni[9], Arianna Gazzi[3,10], Flavia Vitale[11], Julia Somers[12], Emek Demir[12], Serap Suzuk Yildiz[2], Hasan Nazir[13], Jean-Charles Grivel[14], Davide Bedognetti[4,15,16] Andrea Crisanti[17], Kamil Can Akcali[1,18], Yury Gogotsi[5]*, Lucia Gemma Delogu[3]*, Açelya Yilmazer[1,3]*

[1] *Stem Cell Institute, Ankara University, Balgat, Ankara, Turkey*

[2] *Ministry of Health General Directorate of Public Health, Microbiology References Laboratory, Ankara, Turkey*

[3] *Department of Biomedical Sciences, University of Padua, Padua, Italy*

[4] *Cancer Research Department, Sidra Medicine, Doha, Qatar*

[5] *Department of Biomedical Engineering, Ankara University, Golbasi, Ankara, Turkey*

[6] *A.J. Drexel Nanomaterials Institute and Department of Materials Science and Engineering, Drexel University, Philadelphia, Pennsylvania, USA*

[7] *Department of Biology, Gazi University, Ankara, Turkey*

[8] *Department of Virology, Faculty of Veterinary Medicine, Ankara University, Ankara, Turkey*

[9] *La Jolla Institute for Immunology, La Jolla, CA, USA*

[10] *Department of Chemical and Pharmaceutical Sciences, University of Trieste, Trieste, Italy*

[11] *Department of Neurology, Bioengineering, Physical Medicine & Rehabilitation, Center for Neuroengineering and Therapeutics, University of Pennsylvania, Philadelphia, Pennsylvania, USA*

[12] *Oregon Health & Sciences Univerity, Department of Molecular and Medical Genetics, Portland, Oregon, USA*

[13] *Department of Chemistry, Ankara University, Tandogan, Ankara, Turkey*

[14] *Deep Phenotyping Core, Sidra Medicine, Doha, Qatar*

[15] *Department of Internal Medicine and Medical Specialties (DiMI), University of Genoa, Genoa, Italy*

[16] *College of Health and Life Sciences, Hamad Bin Khalifa University, Doha, Qatar*

[17] *Department of Molecular Medicine, Padua University Hospital, Padua, Italy*

[18] *Department of Biophysics, Faculty of Medicine, Ankara University, Ankara, Turkey*

# equal contribution

* corresponding authors:

ayilmazer@ankara.edu.tr, luciagemma.delogu@unipd.it, gogotsi@drexel.edu

Content:

1. Materials and methods

MAX Precursor Synthesis

To prepare the MAX precursors, TiC (<2 μm, Alfa Aesar, 99.5%), Mo (-250 mesh, Alfa Aesar, 99.9%), Ta (-325 mesh, Alfa Aesar, 99.97%), Nb (-325 mesh, Beantown Chemicals, 99.99%), Ti (-325 mesh, Alfa Aesar, 99.5%), Al (-325 mesh, Alfa Aesar, 99.5%), and graphite (-325 mesh, Alfa Aesar, 99%) powders were utilized. For Ti_3AlC_2, a 2:1:1 atomic ratio of TiC:Ti:Al (50 g) was mixed. To produce $Mo_2Ti_2AlC_3$, a 2:2:1.3:2.7 atomic ratio (10 g) of Mo:Ti:Al:C powders were mixed. To synthesize Ta_4AlC_3, a 4:1:3 atomic ratio (7 g) of Ta:Al:C powders were utilized. For Nb_4AlC_3, a 4:1.1:2.7 atomic ratio (10 g) of Nb:Al:C was used. All aforementioned mixtures were mixed in a 2:1 ball:powder weight ratio using 5 mm alumina balls. The mixtures were ball milled at 60 rpm for 24 hours prior to synthesis.

The high-temperature annealing reactions were conducted in a Carbolite furnace, using heating and cooling rates of 3 °C, along with 200 cm^3 min^{-1} flow of ultra-high purity Ar (99.999%). To synthesize Ti_3AlC_2, the mixture was heated to 1400 °C for 2 h. For $Mo_2Ti_2AlC_3$, the powders were heated to 1600 °C for 4 h. To produce Ta_4AlC_3, the powders were heated to 1400 °C for 8 And for Nb_4AlC_3, the mixture was heated to 1650 °C for 4 h. After cooling, the sintered blocks were milled using a TiN-coated bit and sieved through a 400 mesh sieve, resulting in a final particle size <38

μm. All experiments conducted in this study used a single batch of MAX to eliminate any artifacts from variation between MAX synthesis batches.

MXene Synthesis

To selectively etch Al from the MAX phases to produce MXenes, HF (Acros Organics, 48-50 wt. %; 29 M), HCl (Fisher Scientific, 37 wt. %; 12 M), and deionized (DI) water (15 MΩ resistivity) was utilized. For the synthesis of all MXenes in this study, Teflon coated stir bars were utilized with at 300 rpm stirring rate. $Ti_3C_2T_x$ was synthesized by etching 1.0 g Ti_3AlC_2 in a 1:3:6 volumetric ratio (20 mL total) of HF:H_2O:HCl for 24 hours at 35 °C. To produce $Mo_2Ti_2C_3T_x$, 1.0 g $Mo_2Ti_2AlC_3$ was added to 20 mL 48-50 wt.% HF for 96 hours at 55 °C. To synthesize $Ta_4C_3T_x$, 1.0 g Ta_4AlC_3 was added to 20 mL 48-50 wt.% HF for 72 hours at 35 °C. $Nb_4C_3T_x$ was produced by adding 1.0 g of Nb_4AlC_3 to 20 mL 48-50 wt.% HF and stirred for 120 hours at 35 °C. After the appropriate etching time, the MXenes were washed by centrifugation using DI water. Briefly, the mixtures were added to 150 mL DI H_2O, then centrifuged at 3,500 rpm for 10 min. The acidic supernatant (clear) was decanted; the multilayer MXene remained as sediment. New DI H_2O was added, the sediment redispersed, and the process repeated. These cycles were repeated eight times to ensure that all residual acid was removed from the multilayer MXene.

To delaminate the MXenes, and produce a stable colloidal solution, the multilayer MXenes were added to 20 mL of a 5 wt. % TMAOH solution (TMAOH; Sigma Aldrich, 25 wt. % in H_2O). The MXenes were stirred for 12 h at 300 rpm at 35 °C. Afterwards, the mixtures were placed into 50 mL centrifugation tubes. DI water was added, and the samples were centrifuged at 10,000 rpm for 20 min. The supernatant (clear) was decanted, with the MXenes redispersed in fresh DI water. This process was

repeated five times to ensure that all excess TMAOH was removed. After the final cycle, the MXenes were fully redispersed in 50 mL DI water, then centrifuged at 3,500 rpm for 10 minutes. The supernatant (dark) was carefully collected, then centrifuged again at 3,500 rpm for 10 min, the supernatant (dark) was collected for use. This procedure ensured that only single-flake MXene remained in the solution. A known volume of this solution was vacuum filtered on Celgard membranes (64 nm pore size, 3501 coated polypropylene), to produce free-standing films for X-ray diffraction (XRD). By measuring the weight of the produced films, the colloidal solution concentration was determined.

Material Characterization

XRD patterns of the powders and films were collected on a Rigaku MiniFlex600 (40 kV and 15 mA) diffractometer using Cu Kα radiation. The conditions were as follows: (i) for the MAX powder, step scan 0.02, 3–80 (2θ), step time of 1 s; (ii) for the MXene films, a step scan of 0.03, 3–70 (2θ), step time of 0.5 s was used.

Scanning electron microscopy (SEM) was conducted on a dual-beam focused ion beam (Strata DB235, FEI). The MXene flakes were drop-cast onto an anodized alumina substrate. Pt was deposited onto the flake and substrate to minimize charging. DLS (Zetasizer Nano ZS, Malvern Instruments) was performed to analyze MXene flake size distribution. Three measurements were taken of each sample and the average value was reported.

Cell Culture

Jurkat cells were grown in 75 cm^2 flasks at 37 °C, 5% CO_2, in DMEM medium (Invitrogen, CA, USA) containing 10% FBS (Invitrogen, CA, USA), and 1% P/S (Invitrogen, CA, USA). The day before exposure to particles, cells were seeded at 10^5 cells/well in 24-well plates. Vero E6 cells were cultured in high-glucose DMEM medium (Invitrogen, CA, USA) containing 10% FBS (Invitrogen, CA, USA), and 1% P/S (Invitrogen, CA, USA). Cells were maintained at 37 °C, 5% CO_2. For viral infection experiments, African green monkey kidney Vero E6 cell line was purchased from ATCC and maintained in DMEM media containing 10% FBS and 1% antibiotics. Four local SARS-CoV-2 isolates were used in this study and genotype details including GISAID classifications are given in Figure 2B. Viral particles were propagated in Vero E6 cells. All virus-related experiments were performed at Biosafety Level 3 laboratories.

Isolation of PBMCs

PBMCs were harvested from ethylenediaminetetraacetic acid (EDTA)-venous blood from informed healthy donors (25–50 years old) using a Ficoll-Paque (GE Healthcare, CA, USA) standard separation protocol. Informed signed consent was obtained from all the donors. Cell separation and experiments were performed immediately after the blood draw. PBMCs were cultured in 24-well plates in RPMI 1640 medium (Invitrogen, CA, USA), supplemented with 10% heat-inactivated FBS (Invitrogen, CA, USA), 1% P/S (Life Technologies). 1% L-Glutamine (Life Technologies). In addition, EtOH 70% was used as positive control for cell death, while 2 µg/ml LPS (Life Technologies) or 10 µg/ml ConA (Life Technologies) were used as positive control for cell activation.

Flow Cytometer Analysis

Cells were seeded at 10^6 cells/well in 24-well plates, and the day before the experiment cells were exposed to 50 µg/mL $Ti_3C_2T_x$. Cell viability was assessed by means of staining with Fixable Viability Stain 780 (BD Biosciences). EtOH 70% was used as positive control.

To assess PBMC activation after treatment with $Ti_3C_2T_x$, CD25, CD69, and HLA-DR (PE-conjugated anti-CD25, M-A251 clone; PE-Cy7-conjugated anti-CD69, FN50 clone, BV421-conjugated anti-HLA-DR, G46-6 clone; BD Bioscience) were used as activation markers. Lypopolisaccharides (LPS, 2 µg/mL, Life Technologies) or concanavalin A (ConA, 10 µg/mL, Life Technologies) were used as positive control for cell activation in monocytes and T cells, respectively. Staining was performed in the dark for 20 min. Cells were processed by flow cytometry (BD LSRFortessa™ FACS Canto II, BD Bioscience), and data were analyzed by FlowJo™ Software[1].

PBMC staining and gating strategy by flow cytometry

PBMCs were stained with FITC-conjugated anti-CD3 (UCHT1 clone; BD Biosciences), BV605-conjugated anti-CD4 (RPA-T4 clone; BD Biosciences), BV786-conjugated anti-CD14 (M5E2 clone; BD Biosciences), and BV711-conjugated anti-CD16 (3G8 clone; BD Biosciences).

Gating strategy was performed as described in Figure S6E. Briefly, doublets and cell debris were excluded trough the gating strategy and specific subpopulations were determined. Specifically: CD4 T cells (CD3+ CD4+), CD8 T cells (CD3+ CD4-), Classical (C.) monocytes (CD3− CD14+ CD16-), Intermediate (Int.) monocytes (CD3− CD14+ CD16+), Non-classical (N.C.) monocytes (CD3− CD14- CD16+).

Single-cell mass cytometry analysis

Single-cell mass cytometry analysis was performed on isolated PBMCs, collected as described above, seeded at a concentration of 4×10^6 cells/well in 6-well plates. PBMCs were incubated with 50 µg/mL of $Ti_3C_2T_x$ for 24 h or left untreated (negative control). LPS at 0.5 µg/mL (Sigma – Aldrich, Missouri, USA) and EtOH 70% were used as positive controls. Six hours prior to the treatment end, cells were co-incubated with 10 µg/mL Brefeldin A (Invitrogen, CA, USA). After the incubation, PBMCs were washed with PBS supplemented with 0.5 M EDTA and 5% Fetal Calf Serum (FCS).

Cells were then barcoded using Cell-ID 20-Plex Pd Barcoding Kit (Fluidigm, CA, USA). The barcoded samples were stained with Cell-ID Cisplatin (1:1000, Fluidigm, CA, USA), Maxpar Human Peripheral Blood Phenotyping and Human Intracellular Cytokine I Panel Kits (Fluidigm, CA, USA) following the manufacturer instructions. To this end, cells were fixed and permeabilized with 1X Fix I Buffer and 1X Barcode Perm Buffer obtaining a uniform cell labeling with the palladium barcode. Thanks to the barcoding process, samples were pooled together and re-suspended into a 5 ml polystyrene round-bottom tube using the Maxpar Cell Staining Buffer.

The surface marker antibody mix (1:100 dilutions for each antibody) was added to the sample. Cells were then carefully mixed and incubated for 30 min at room temperature. At the end of the incubation, samples were washed twice with Maxpar Cell Staining Buffer, and fixed by incubation with 1.6% paraformaldehyde for 10 min. After this, cells were washed twice with Maxpar Perm-S Buffer, centrifuged for 10 min at 1000×g, resuspended in 400 µl of Maxpar Perm-S Buffer, and incubated with cytoplasmic/secreted antibody mix for 30 min (1:100 dilutions for each antibody). Following the incubation, cells were washed twice with Maxpar Cell Staining Buffer, and stained overnight using 0.125 µM Cell-ID Intercalator-Ir solution. The day after,

samples were washed twice with Maxpar Cell Staining Buffer, re-suspended with 2 ml of Maxpar water, and filtered before data acquisition using a 0.22 μm cell strainer cap to remove possible cell clusters or aggregates. Data were analyzed using mass cytometry platform CyTOF2 (Fluidigm Corporation, CA, USA).

CyTOF data analysis was performed as described before[2, 3]. Briefly, background was subtracted and FCS files were normalized and analyzed by Cytobank. Doublets, cell debris, and dead cells were excluded trough the gating strategy using Cell-ID Intercalator-Ir and LD. PBMCs subsets and specific subpopulations were determined as portrayed in Figure 1E. Specifically: T cells (CD45+ CD19- CD3+), Naïve Th. Cells (CD3+ CD4+ CD45RA+ CD27+ CD38− HLADR−), Effector Th. cells (CD3+ CD4+ CD45RA+ CD27− CD38− HLADR−), Activated Th. cells (CD3+ CD4+ CD38+ HLADR+), Naïve CT cells (CD3+ CD8+ CD45RA+ CD27+ CD38− HLADR−), Effector CT cells (CD3+ CD8+ CD45RA+ CD27− CD38− HLADR−), Activated CT cells (CD3+ CD8+ CD38+ HLADR+), C. monocytes (CD45+ CD3− CD19− CD20− HLADR+ CD14+), int. monocytes (CD45+ CD3− CD19− CD20− HLADR+ CD14dim CD16+), N.C. monocytes (CD45+ CD3− CD19− CD20− CD11c- CD14- CD16+), mDCs (CD45+ CD3− CD19− CD20− CD14− HLA− DR+ CD11c+ CD123−), pDCs (CD45+ CD3− CD19− CD20− CD14− CD11c− HLADR+ CD123+), NK cells (CD45+ CD3− CD19− CD20− CD14− CD11c- CD38+ CD16+), B cells (CD3- CD20+ CD19+), naïve B cells (CD27−), plasma B cells (HLADR- CD38+). The heat map visualization created with Cytobank, allowed the comparison between the marker fluorescence of the treated populations with mean fluorescent intensity towards the untreated control. Moreover, viSNE, a Cytobank tool implemented for cytometry analysis was employed. The t-stochastic neighbor embedding (t-SNE) shows single cells in a two- or three-dimensional plot, on the basis of their relationships. In order to

characterize the viSNE map, 10 cell surface markers were used (i.e. CD3, CD4, CD8a, CD11c, CD14, CD16, CD19, CD20, CD123, and HLA-DR).

Cytokine data were analyzed using the viSNE tool, and displayed as plots of the expression intensity of the studied cytokines (i.e., IL-6, TNF-α, IL-17a, IL17f, IFN-γ, Perforin, and GrB), and heatmaps of mean marker expression ratio for cytokines that displayed modulations upon $Ti_3C_2T_x$ treatment.

The specific clone of each antibody used for mass cytometry has been provided in Table S3.

Detection of TNF α

TNF-α levels were evaluated in the supernatant of PBMCs treated with Ti3C2Tx (50 µg mL-1) for 24h, or lipopolysaccharide (LPS, a strong immunostimulatory molecule) plus Ti3C2Tx, LPS alone, cell control samples were left untreated. The Cytometric Bead Array (CBA) immunoassay kit (BD Biosciences, USA) was used to quantify TNF-α concentration following the manufacturer instructions. Data were acquired in a BD LRS Fortessa flow cytometry system (BD Biosciences, San Jose, CA, USA) and analyses performed using BD FCAP Array v3.0 software (BD Biosciences, San Jose, CA, USA). The standard curve was determined using a five-parameter logistic (5-PL) equation. The results were based on standard concentration curve and expressed as picogram per milliliter (pg/mL).

Luminex analysis

To evaluate the impact of MXenes on cytokine release by PBMCs, cells were incubated for 24 h with 50 µg/mL of $Ti_3C_2T_x$. ConA, 4 µg/mL (Sigma) and LPS, 2 µg/mL (Sigma) were used as positive controls, while samples incubated with medium

alone were used as negative controls. Supernatants were collected and analysed by Luminex technology using Bio-Plex Pro Human Chemokine 40-plex Panel (Bio-Rad) to measure C-C Motif Chemokine Ligand (CCL) 21 (CCL21), chemokine (C-X-C motif) ligand (CXCL) 13 (CXCL13), CCL27, CXCL5, CCL11, CCL24, CCL26, C-X3-C Motif Chemokine Ligand 1 (CX3CL1), CXCL6, granulocyte macrophage-colony stimulating factor (GM-CSF), CXCL1, CXCL2, CCL1, interferon gamma (IFN-γ), interleukin (IL)-1β, IL-2, IL-4, IL-6, CXCL8, IL-10, IL-16, CXCL10, CXCL11, CCL2, CCL8, CCL7, CCL13, CCL22, macrophage migration inhibitory factor (MIF), CXCL9, CCL3, CCL15, CCL20, CCL19, CCL23, CXCL16, CXCL12, CCL17, CCL25 and tumor necrosis factor (TNF)-α. 5-parameter-Logistic regressions with a power low variance weighing were calculated for each cytokine standard with a recovery range of 70-130% using Bioplex Manager V6.2 (BioRad). Concentration falling within the recovery range, expressed in pg/ml were extrapolated from the median fluorescence intensity of each cytokine bead set. For analytes above or below the standard recovery ranges, upper and lower limits of quantification computed from the standard curves were substituted. Data were then Log2 transformed and compared across experiments by fitting a general ANOVA model with contrast between groups; *p* values were corrected using Benjamini and Hochberg false discovery rate, FDR; statistically significant *p* value cut-off was set at FDR $p < 0.05$.

Molecular Docking

Water and ligand molecules were removed from protein structures using UCSF Chimera Software Version 1.14[4]. All protein structures were downloaded from the Protein Data Bank. Protein models and $Ti_3C_2T_x$ ligand were converted to PDBQT file format using parameters defined by default in the AUTODOCK 4.0[5] program, and

blind docking calculations were made for each protein by defining grid box maximum and grid space 1 Å. Since all conformations are very close to each other (± 0.01 kcal / mol), the first conformation was taken as basis in all analyzes. Discovery Studio's academic version was used for the preparation of the visuals of the calculations and additional calculations[6].

Viral Infection

Vero E6 cells were seeded onto 96-well plates at confluency. Cells were incubated with MXenes (at different dilutions from a stock solution of 1.1 mg/mL) and SARS-CoV-2 (MOI 0.1). Cell viability was obtained after 48 h by using crystal violet staining. Briefly, cells were first incubated in 10% formaldehyde. Following this decontamination, plates were washed under running water and stained with Crystal. Violet (Sigma) for 20 min. EtOH was added in order to solubilize the stain and absorbance values were obtained at 495 nm wavelength. Percentage of cell viability was obtained following normalization against untreated control cells.

qRT-PCR analysis

Following treatment, cell culture supernatants were removed and RNA was isolated via MPLC Total Nucleic Acid Isolation Kit (Roche) using automated MagNA Pure LC Instrument (Roche). One-step qRT-PCR was performed using the Transcriptor One-Step RT-PCR Kit (Roche). A standard curve was constructed in order to calculate viral copies per µL. Primer seqeunces (2019-nCoV_N1) were obtained from the Division of Viral Diseases, National Center for Immunization and Respiratory Diseases, Centers for Disease Control and Prevention, Atlanta, GA, USA.

LC-MS/MS Analysis

Vero E6 cells were incubated with $Ti_3C_2T_x$ (50 μg/mL) in 6 well-plates for 24 h. Subsequently, cells were washed with cold PBS and cell pellets were obtained. Total protein concentration was obtained using BCA assay (Thermo). LC-MS/MS analysis was performed at the proteomic facility of Acibadem Labmed (Turkey). Protein profiling was performed using nano Acquity ultra performance liquid chromatography coupled with LC-MS/MS system on Synapt instrument (Waters) as described before[7, 8].

Functional Annotation

For the analyses the proteins with $p<0.05$ and fold change (FC)≥1 based on log2 expression value were assigned as differentially expressed. Gene Ontology (GO) is used to annotate the proteins[9]. The three sub-ontologies of biological process (BP), cellular component (CC), and molecular function (MF) were identified. To obtain a comprehensive functional annotation, different databases were searched. The ontology enrichment and pathway analyses were performed using the DAVID database[10]. Metabolic pathways based on available databases such as KEGG[11] and Reactome[12] were also used to describe the pathway enrichment analyses. The protein-protein interactions network was predicted via String database[13]. The interaction score was set to ≥ 0.4, and the PPI (Protein-Protein Interaction) networks were created. BiomaRt R package was used to combine the datasets[14].

Statistical Analysis

All values are expressed as mean ± ST.D. Comparison between groups was performed by one-way ANOVA, followed by a Tukey's post hoc multiple comparisons where data

were normally distributed. At least three independent samples were analyzed. A value of $p < 0.05$ was considered significant.

2. Supplementary Figures

Figure S1. **Evaluation of the effect of $Ti_3C_2T_x$ on SARS-CoV-2 infection *in silico*.** *In silico* molecular docking analysis of $Ti_3C_2T_x$ against different viral protein domains (6VWW, 6LU7, 6M0J, 6M03, 6VXX and 6VYB) was performed and types of interactions and amino acid residues involved during these interactions were identified.

Figure S2. **Functional annotation of $Ti_3C_2T_x$ treated Vero E6 cells.** Vero E6 cells were treated with $Ti_3C_2T_x$ (50 µg/ml for 4 h) and cellular total proteins were isolated for LC-MS/MS analysis. GO annotation was performed for **A)** biological process (BP) and **B)** molecular function (MF).

Supplementary Figure 3. Full reactome of $Ti_3C_2T_x$ treated cells. Vero E6 cells were treated with $Ti_3C_2T_x$ and cellular total proteins were isolated for LC-MS/MS analysis. Genome-wide overview of the Reactome pathway analysis was performed and the whole reactome image is represented. Scale bar represents p value from 0 to 0.05.

Supplementary Figure 4. Functional annotation of $Ti_3C_2T_x$ treated Vero E6 cells. Vero E6 cells were treated with $Ti_3C_2T_x$ and cellular total proteins were isolated for LC-MS/MS analysis. Network analysis was performed in order to dissect the functional protein associations by the String program for the significantly overlapping proteins

with the SARS-CoV-2 protein interaction map reported in the study by Gordon et al [15]. The jointed lines represent the predicted protein-protein connections and correlations among the network. Differentially expressed proteins of $Ti_3C_2T_x$ treatment shows numerous connections between the proteins.

Figure S5. Viability on Jurkat cells and gating strategy on peripheral blood mononuclear cells. Flow cytometry analysis on Jurkat cells and PBMCs. Jurkat cells were treated with 12.5, 25 and 50 μg/ml of $Ti_3C_2T_x$, while PBMCs were treated with the selected concentration of 50 μg/mL of $Ti_3C_2T_x$ for 24 h or left untreated (Unt). EtOH 70% was used as a positive control to induce cell death. LPS (2 μg/mL) and ConA (10 μg/mL) were used as positive controls for cell differentiation analysis. **A)** Jurkat cells were stained with Live/Dead staining and cell death was evaluated and expressed as percentage of total cell number. **B)** Representative flow cytometric dot plot of Jurkat cells. **C)** Histogram plots showing live and dead Jurkat cells. **D)** Pseudocolor plot showing the gating strategy applied to flow cytometry analyses of PBMCs. **E)** Representative flow cytometric dot plot of PBMCs untreated (Unt) or treated with: EtOH 70%, LPS (2 μg/mL), ConA (10 μg/mL), or $Ti_3C_2T_x$ (50 μg/mL). Data are presented as mean ± ST.D. of three independent samples.

Figure S6. Viability of PBMCs and monocytes. Cell viability and activation staining analysis by flow cytometry and CyTOF. Cells were treated with $Ti_3C_2T_x$ (50 μg/mL) for 24 h or left untreated (Unt). EtOH 70% was used as a positive control to induce cell death. Cells were stained with Fixable Viability Staining 780 to evaluate necrosis. **A)** Representative flow cytometric analysis for cell viability staining of PBMCs. **B)** Bar graph of cisplatin (LD) mean marker expression ratio for all CD45+ PBMCs. **C)** Bar

graph of cisplatin (LD) mean marker expression ratio for all T cell, monocyte, DC, NK, and B cell subpopulations. Heatmaps and viSNE plots were generated on the concatenated files. Data are presented as mean ± ST.D. of three independent samples. **D)** Representative flow cytometric analysis (left panel) and histogram plot (right panel) for cell viability staining of CD4 T cells. **E)** Representative flow cytometric analysis (left panel) and histogram plot (right panel) for cell viability staining of CD8 T cells. **F)** Representative flow cytometric analysis for cell viability staining of monocytes. **G)** Representative flow cytometric analysis (left panel) and histogram plot (right panel) for cell viability staining of C. monocytes. **H)** Representative flow cytometric analysis (left panel) and histogram plot (right panel) for cell viability staining of Int. monocytes. **I)** Representative flow cytometric analysis (left panel) and histogram plot (right panel) for cell viability staining of N.C. monocytes. Data are presented as mean ± ST.D. of three independent samples.

Figure S7. Analysis of activation on peripheral blood mononuclear cells and monocytes. Cell activation staining analysis by flow cytometry. Cells were treated with 50 μg/ml $Ti_3C_2T_x$ for 24h or left untreated (Unt). LPS 2 μg/ml was used as a positive control for PBMCs while ConA 10 μg/ml was used as positive control for T cells. To evaluate cell activation, PBMCs and monocytes were stained with CD25-PE and CD69-PE-Cy7 **A)** Representative flow cytometric analysis for cell activation staining of PBMCs. **B)** Representative flow cytometric analysis (left panel) and histogram plot (right panel) for cell activation staining of CD4 T cells. **C)** Representative flow cytometric analysis (left panel) and histogram plot (right panel) for cell activation staining of CD8 T cells. **D)** Representative flow cytometric analysis (left panel) and histogram plot (right panel) for cell activation staining of monocytes. **E)** Representative

flow cytometric analysis (left panel) and histogram plot (right panel) for cell activation staining of C. monocytes. **F)** Representative flow cytometric analysis (left panel) and histogram plot (right panel) for cell activation staining of Int. monocytes. **G)** Representative flow cytometric analysis (left panel) and histogram plot (right panel) for cell activation staining of N.C. monocytes. **H)** Representative flow cytometric analysis for CD25-PE staining in PBMCs treated with 50 µg/mL of $Ti_3C_2T_x$. Cell activation was expressed as % of positive cells. **I)** TNF-α concentration measured in the supernatant of PBMCs treated with $Ti_3C_2T_x$ (50 µg/mL) using BD Cytometric Bead Array(CBA) Kit. Data are presented as mean ± SD of three independent samples. *, $p < 0.05$; **, $p < 0.01$; ***, $p < 0.001$; **** $p < 0.0001$ (Ordinary one-way ANOVA).

Figure S8. Analysis of HLA-DR on peripheral blood mononuclear cells and monocytes. HLA-DR staining analysis by flow cytometry. Cells were treated with 50 µg/ml $Ti_3C_2T_x$ for 24h or left untreated (Unt). LPS 2 µg/ml and ConA 10 µg/ml were used as positive control. **A)** PBMCs were stained with BV421-HLA-DR, and HLA-DR expression was evaluated in PBMCs, CD4 T cells, and CD8 T cells. Results are expressed as percentage of total cell number. **B)** Representative flow cytometric analysis for HLA-DR staining of PBMCs, CD4 T cells, and CD8 T cells. **C)** Histogram plots showing HLA-DR staining of PBMCs, CD4 T cells, and CD8 T cells. **D)** Monocytes were stained with BV421 HLA-DR and HLA-DR expression was evaluated in monocytes as well in monocyte subpopulations (i.e., C. monocytes, Int. monocytes and N.C. monocytes). Results are expressed as percentage of total cell number. **E)** Representative flow cytometric analysis for HLA-DR staining of monocytes and monocyte subpopulations (i.e., C. monocytes, Int. monocytes and N.C. monocytes).

F) Histogram plots showing HLA-DR staining of monocytes and monocyte subpopulations (i.e., C. monocytes, Int. monocytes and N.C. monocytes).

Figure S9. **$Ti_3C_2T_x$ impact on peripheral blood mononuclear cell subpopulations at single-cell level.** Blood from healthy donors was drawn, and PBMCs were isolated and incubated with 50 µg/ml $Ti_3C_2T_x$ for 24h and stained for mass cytometry analysis. LPS 2 µg/ml was used as a positive control. **A-G)** Bar graphs reporting the immune response to $Ti_3C_2T_x$ of three biological replicates for **A)** IL-6, **B)** TNF-α, **C)** IFN-γ, **D)** Perforin, **E)** GrB, **F**) IL-17a, and **B)** IL-17f and immune subpopulations identified. Data are presented as mean ± ST.D. of three independent samples. Statistical differences: *p<0.05; **p<0.01; ***p<0.001 (One-way ANOVA and Tukey's multiple comparison test).

Figure S10. Immune cell subpopulations gating strategy. Dot plots showing the gating strategy used for the identification of the different immune cell subpopulations by CyTOF.

References

[1] Becton, Dickinson and Company, Ashland, OR 2019.

[2] M. Orecchioni, D. Bedognetti, L. Newman, C. Fuoco, F. Spada, W. Hendrickx, F.M. Marincola, F. Sgarrella, A.F. Rodrigues, C. Menard-Moyon, G. Cesareni, K. Kostarelos, A. Bianco, L.G. Delogu, Single-cell mass cytometry and transcriptome profiling reveal the impact of graphene on human immune cells, Nat. Commun., 8 (2017) 1109.

[3] S.C. Bendall, E.F. Simonds, P. Qiu, A.D. Amir el, P.O. Krutzik, R. Finck, R.V. Bruggner, R. Melamed, A. Trejo, O.I. Ornatsky, R.S. Balderas, S.K. Plevritis, K. Sachs, D. Pe'er, S.D. Tanner, G.P. Nolan, Single-cell mass cytometry of differential immune and drug responses across a human hematopoietic continuum, Science, 332 (2011) 687-696.

[4] E.F. Pettersen, T.D. Goddard, C.C. Huang, G.S. Couch, D.M. Greenblatt, E.C. Meng, T.E. Ferrin, UCSF Chimera-a visualization system for exploratory research and analysis, J. Comput. Chem., 25 (2004) 1605-1612.

[5] G.M. Morris, R. Huey, W. Lindstrom, M.F. Sanner, R.K. Belew, D.S. Goodsell, A.J. Olson, AutoDock4 and AutoDockTools4: Automated docking with selective receptor flexibility, J .Comput. Chem., 30 (2009) 2785-2791.

[6] 2016.

[7] H. Taheri, M.A. Unal, M. Sevim, C. Gurcan, O. Ekim, A. Ceylan, Z. Syrgiannis, K.C. Christoforidis, S. Bosi, O. Ozgenç, M.J. Gómez, M. Turktas Erken, Ç. Soydal, Z. Eroğlu, C.V. Bitirim, U. Cagin, F. Arı, A. Ozen, O. Kuçuk, L.G. Delogu, M. Prato, Ö. Metin, A. Yilmazer, Photocatalytically active graphitic carbon nitride as an effective and safe 2D material for in vitro and in vivo photodynamic therapy, Small, 16 (2020) 1904619.

[8] W. Zhu, R. Michalsky, Ö. Metin, H. Lv, S. Guo, C.J. Wright, X. Sun, A.A. Peterson, S. Sun, Monodisperse Au nanoparticles for selective electrocatalytic reduction of CO_2 to CO, J. Am. Chem. Soc., 135 (2013) 16833-16836.

[9] M. Ashburner, C.A. Ball, J.A. Blake, D. Botstein, H. Butler, J.M. Cherry, A.P. Davis, K. Dolinski, S.S. Dwight, J.T. Eppig, M.A. Harris, D.P. Hill, L. Issel-Tarver, A. Kasarskis, S. Lewis, J.C. Matese, J.E. Richardson, M. Ringwald, G.M. Rubin, G.

Sherlock, Gene ontology: tool for the unification of biology. The Gene Ontology Consortium, Nat. Genet., 25 (2000) 25-29.

[10] G. Dennis, B.T. Sherman, D.A. Hosack, J. Yang, W. Gao, H.C. Lane, R.A. Lempicki, DAVID: Database for annotation, visualization, and integrated discovery, Genome Biol, 4 (2003).

[11] M. Kanehisa, S. Goto, S. Kawashima, Y. Okuno, M. Hattori, The KEGG resource for deciphering the genome, Nucleic Acids Res., 32 (2004) D277-D280.

[12] G. Joshi-Tope, M. Gillespie, I. Vastrik, P. D'Eustachio, E. Schmidt, B. de Bono, B. Jassal, G.R. Gopinath, G.R. Wu, L. Matthews, S. Lewis, E. Birney, L. Stein, Reactome: a knowledgebase of biological pathways, Nucleic Acids Res., 33 (2005) D428-D432.

[13] D. Szklarczyk, A.L. Gable, D. Lyon, A. Junge, S. Wyder, J. Huerta-Cepas, M. Simonovic, N.T. Doncheva, J.H. Morris, P. Bork, L.J. Jensen, C. Mering, STRING v11: protein-protein association networks with increased coverage, supporting functional discovery in genome-wide experimental datasets, Nucleic Acids Res., 47 (2019) D607-D613.

[14] S. Durinck, Y. Moreau, A. Kasprzyk, S. Davis, B. De Moor, A. Brazma, W. Huber, BioMart and Bioconductor: a powerful link between biological databases and microarray data analysis, Bioinformatics, 21 (2005) 3439-3440.

[15] D.E. Gordon, G.M. Jang, M. Bouhaddou, J. Xu, K. Obernier, K.M. White, M.J. O'Meara, V.V. Rezelj, J.Z. Guo, D.L. Swaney, T.A. Tummino, R. Hüttenhain, R.M. Kaake, A.L. Richards, B. Tutuncuoglu, H. Foussard, J. Batra, K. Haas, M. Modak, M. Kim, P. Haas, B.J. Polacco, H. Braberg, J.M. Fabius, M. Eckhardt, M. Soucheray, M.J. Bennett, M. Cakir, M.J. McGregor, Q. Li, B. Meyer, F. Roesch, T. Vallet, A. Mac Kain, L. Miorin, E. Moreno, Z.Z.C. Naing, Y. Zhou, S. Peng, Y. Shi, Z. Zhang, W. Shen, I.T.

Kirby, J.E. Melnyk, J.S. Chorba, K. Lou, S.A. Dai, I. Barrio-Hernandez, D. Memon, C. Hernandez-Armenta, J. Lyu, C.J.P. Mathy, T. Perica, K.B. Pilla, S.J. Ganesan, D.J. Saltzberg, R. Rakesh, X. Liu, S.B. Rosenthal, L. Calviello, S. Venkataramanan, J. Liboy-Lugo, Y. Lin, X.-P. Huang, Y. Liu, S.A. Wankowicz, M. Bohn, M. Safari, F.S. Ugur, C. Koh, N.S. Savar, Q.D. Tran, D. Shengjuler, S.J. Fletcher, M.C. O'Neal, Y. Cai, J.C.J. Chang, D.J. Broadhurst, S. Klippsten, P.P. Sharp, N.A. Wenzell, D. Kuzuoglu-Ozturk, H.-Y. Wang, R. Trenker, J.M. Young, D.A. Cavero, J. Hiatt, T.L. Roth, U. Rathore, A. Subramanian, J. Noack, M. Hubert, R.M. Stroud, A.D. Frankel, O.S. Rosenberg, K.A. Verba, D.A. Agard, M. Ott, M. Emerman, N. Jura, M. von Zastrow, E. Verdin, A. Ashworth, O. Schwartz, C. d'Enfert, S. Mukherjee, M. Jacobson, H.S. Malik, D.G. Fujimori, T. Ideker, C.S. Craik, S.N. Floor, J.S. Fraser, J.D. Gross, A. Sali, B.L. Roth, D. Ruggero, J. Taunton, T. Kortemme, P. Beltrao, M. Vignuzzi, A. García-Sastre, K.M. Shokat, B.K. Shoichet, N.J. Krogan, A SARS-CoV-2 protein interaction map reveals targets for drug repurposing, Nature, 583 (2020) 459-468.

Figure S1

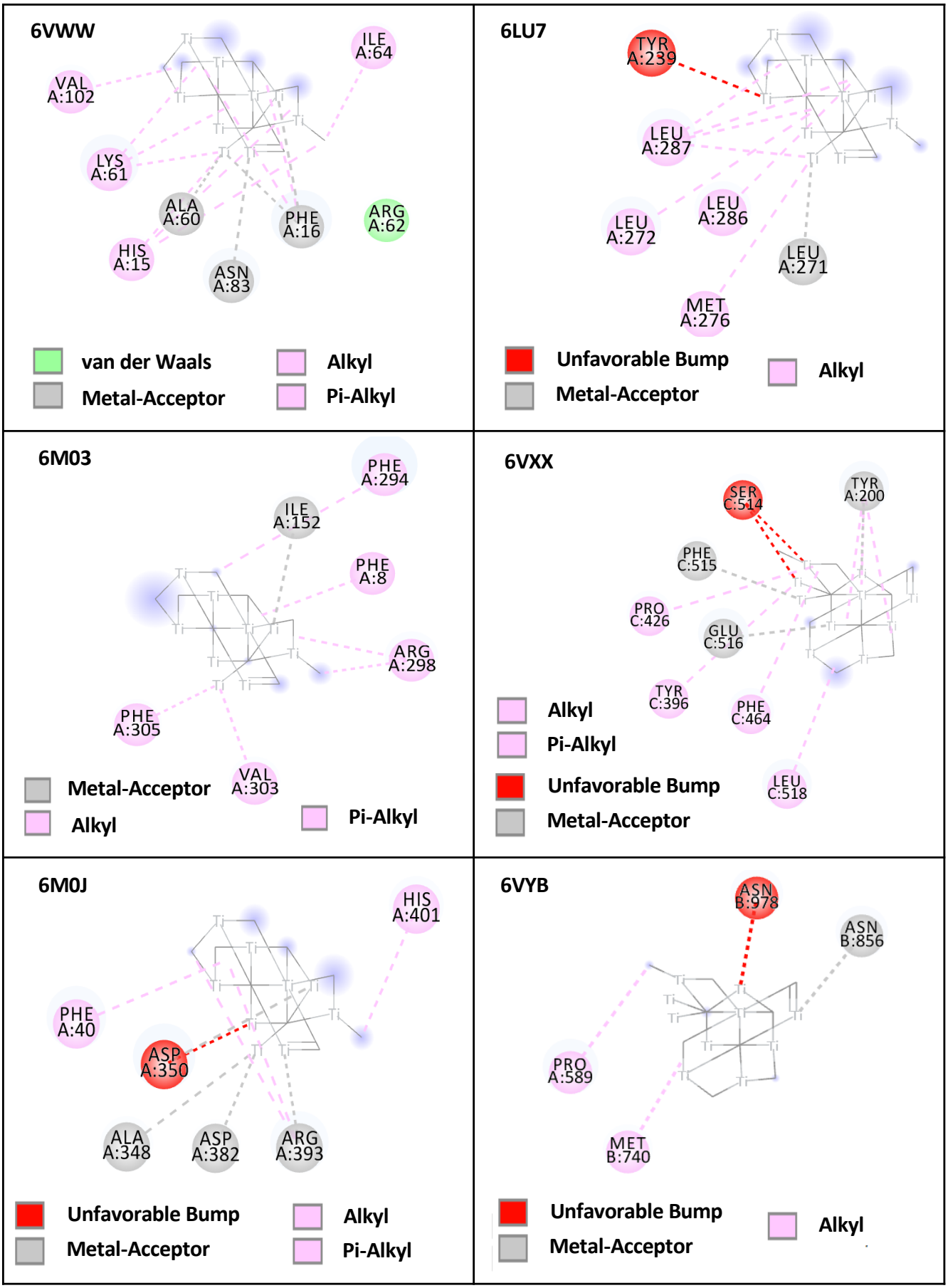
6VWW
ILE A:64
VAL A:102
LYS A:61
ALA A:60
PHE A:16
ARG A:62
HIS A:15
ASN A:83
van der Waals
Alkyl
Metal-Acceptor
Pi-Alkyl
6LU7
TYR A:239
LEU A:287
LEU A:286
LEU A:272
LEU A:271
MET A:276
Unfavorable Bump
Alkyl
Metal-Acceptor
6M03
PHE A:294
ILE A:152
PHE A:8
ARG A:298
PHE A:305
VAL A:303
Metal-Acceptor
Alkyl
Pi-Alkyl
6VXX
SER C:514
TYR A:200
PHE C:515
PRO C:426
GLU C:516
TYR C:396
PHE C:464
LEU C:518
Alkyl
Pi-Alkyl
Unfavorable Bump
Metal-Acceptor
6M0J
HIS A:401
PHE A:40
ASP A:350
ALA A:348
ASP A:382
ARG A:393
Unfavorable Bump
Metal-Acceptor
Alkyl
Pi-Alkyl
6VYB
ASN B:978
ASN B:856
PRO A:589
MET B:740
Unfavorable Bump
Metal-Acceptor
Alkyl

Figure S2

A

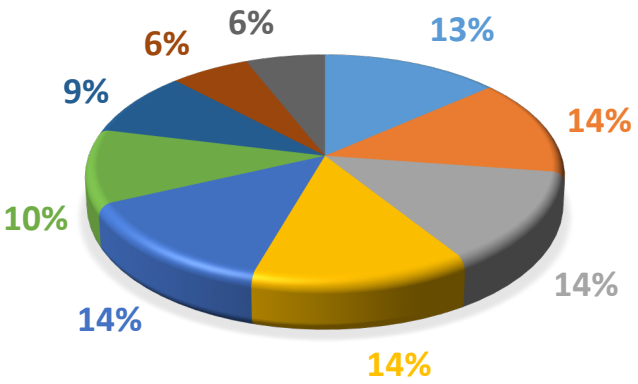

B

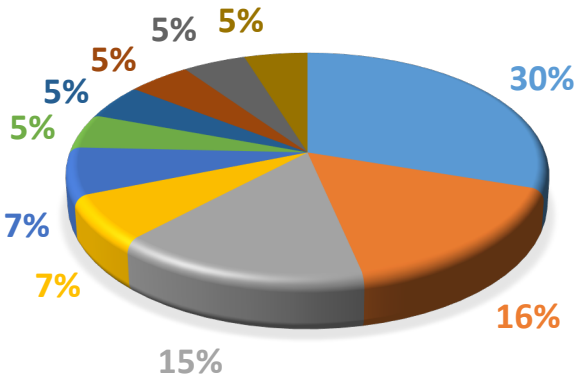

- DNA replication-dependen nucleosome assembly
- DNA replication-independent nucleosome assembly
- DNA-templated transcription inititaion
- negative regulation of megakaryocyte differentiation
- protein heterotetramerization
- intracellular protein transport
- transport
- regulation of transcription DNA-templated

- poly(A) RNA binding
- DNA binding
- ATP binding
- GTP binding
- zinc ion binding
- calcum ion binding
- chromatin binding
- GTPase activity

Figure S3

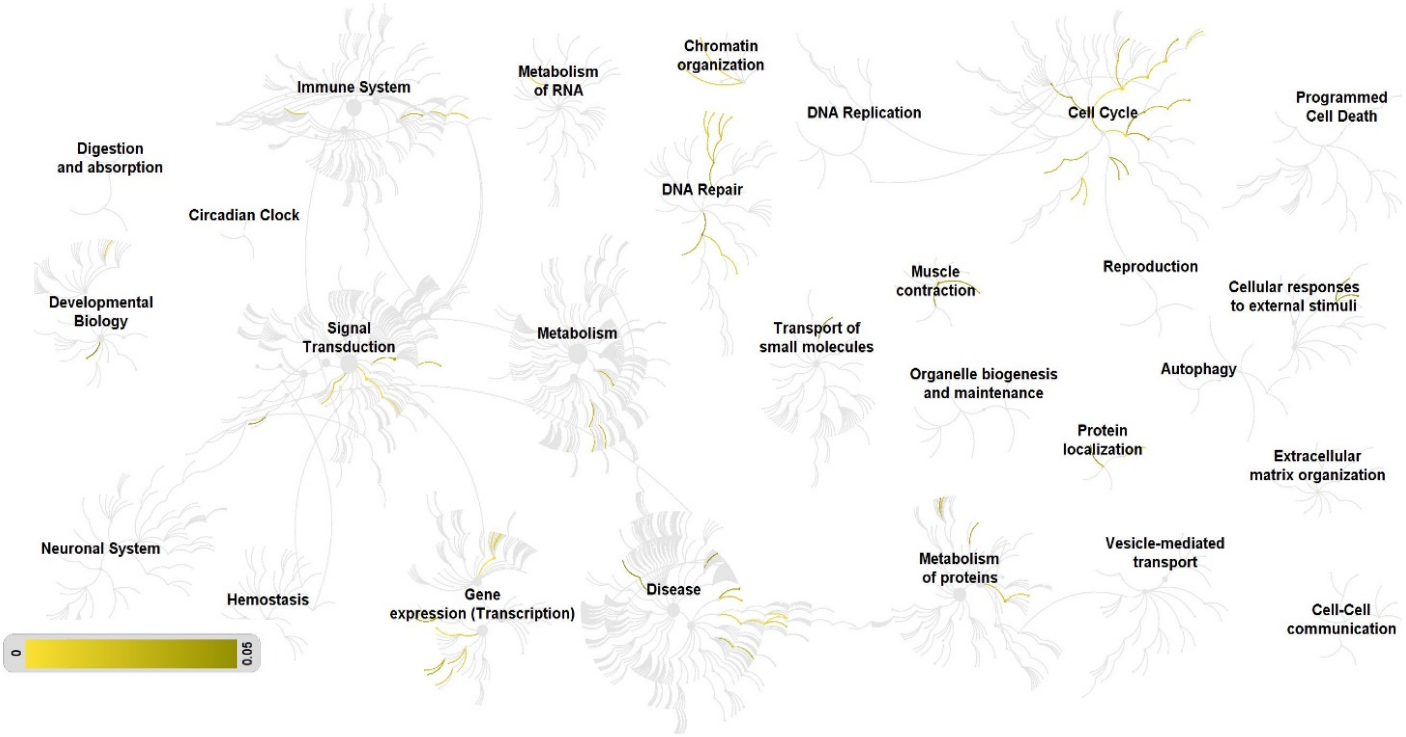
Immune System
Metabolism of RNA
Chromatin organization
DNA Replication
Cell Cycle
Programmed Cell Death
Digestion and absorption
DNA Repair
Circadian Clock
Muscle contraction
Reproduction
Developmental Biology
Signal Transduction
Metabolism
Transport of small molecules
Cellular responses to external stimuli
Organelle biogenesis and maintenance
Autophagy
Protein localization
Extracellular matrix organization
Neuronal System
Metabolism of proteins
Vesicle-mediated transport
Hemostasis
Gene expression (Transcription)
Disease
Cell-Cell communication
0
0.05

Figure S4

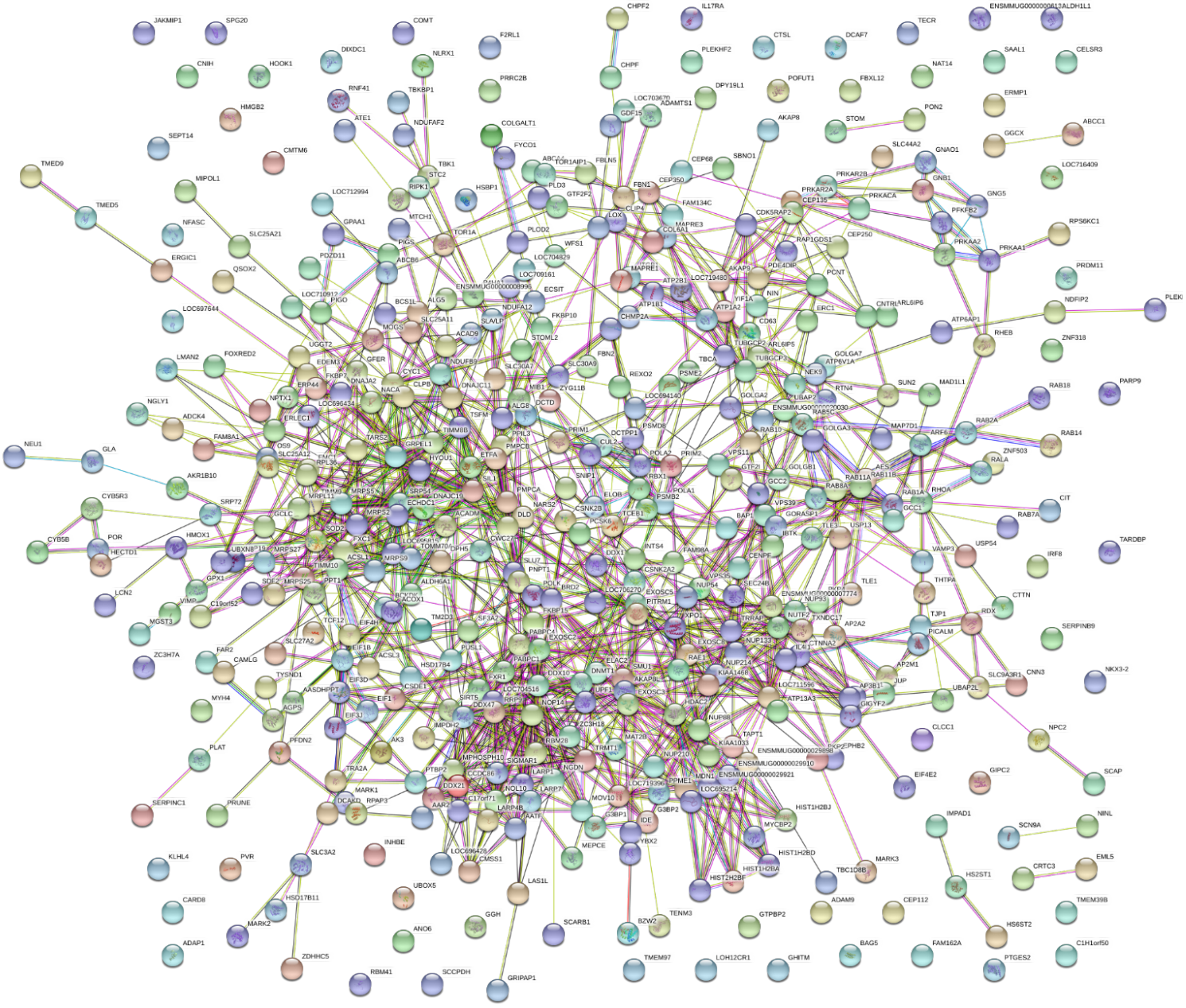
JAKMIP1
SPG20
COMT
CHPF2
IL17RA
ENSMMUG00000000613
ALDH1L1
F2RL1
TECR
DIXDC1
CTSL
DCAF7
CELSR3
CNIH
HOOK1
NLRX1
CHPF
PLEKHF2
SAAL1
NAT14
RNF41
TBKBP1
PRRC2B
DPY19L1
POFUT1
FBXL12
ERMP1
HMGB2
ATE1
NDUFAF2
LOC703670
ADAMTS1
GDF15
AKAP8
STOM
PON2
ABCC1
SEPT14
CMTM6
COLGALT1
FYCO1
SLC44A2
GNAO1
GGCX
TMED9
TBK1
STC2
ABCA7
TOR1AIP1
FBLN5
CEP68
SBNO1
LOC716409
MIPOL1
RIPK1
HSBP1
PLD3
FBN1
CEP350
PRKAR2B
GNB1
TMED5
LOC712994
GTF2F2
CLIP4
FAM134C
PRKAR2A
CEP135
PRKACA
GNG5
MTCH1
LOX
CDK5RAP2
NFASC
GPAA1
TOR1A
MAPRE3
CCDC6
PFKFB2
RPS6KC1
SLC25A21
PIGS
PLOD2
WFS1
RAP1GDS1
CEP250
PRKAA2
PRKAA1
ERGIC1
PDZD11
ABCB6
LOC704829
PDE4DIP
PRDM11
QSOX2
LOC709161
MAPRE1
AKAP9
PCNT
LOC697644
LOC710912
PIGO
ATP2B1
LOC719480
YIF1A
NIN
NDFIP2
PLEKH
ENSMMUG00000008996
ECSIT
ATP1B1
ATP1A2
ERC1
CNTRL
ARL6IP6
NDUFA12
BCS1L
ALG5
SLC25A11
FKBP10
CHMP2A
CD63
ATP6AP1
MOGS
SLAILP
STOML2
RHEB
ACAD9
TUBGCP2
ARL6IP5
ZNF318
UGGT2
FBN2
TUBGCP3
GOLGA7
LMAN2
FOXRED2
EDEM3
GFER
SLC30A7
SLC30A9
TBCA
ATP6V1A
NEK9
SUN2
MAD1L1
PARP9
FKBP7
NDUFB3
CYC1
PSME2
REXO2
RTN4
RAB18
NPTX1
DNAJA2
NACA
CLPB
DNAJC11
MIB1
ZYG11B
LOC694140
GOLGA2
NGLY1
LOC696434
ALG8
DCTD
ENSMMUG00000020030
RAB5C
ADCK4
ERLEC1
TSFM
PRIM1
PSMD8
RAB10
GOLGA3
MAP7D1
RAB2A
NEU1
FAM8A1
TARS2
TIMM8B
PRIM2
ARF6
RAB14
GLA
OS9
GRPEL1
PMPCB
CUL2
DCTPP1
VPS11
ZNF503
SLC25A12
ETFA
HYOU1
POLA2
GTF2I
GOLGB1
RALA
AKR1B10
RPL36
SIL1
SNIP1
RBX1
RAB11A
RAB11B
CYB5R3
MRPL11
MRPS5
SRP54
DNAJC19
PMPCA
ELOB
PSMB2
POLA1
RAB8A
RHOA
SRP72
ECHDC1
NARS2
CSNK2B
VPS39
GCC1
CIT
GCLC
MRPS2
ACADM
DLD
PCSK6
TCEB1
BAP1
GORASP1
RAB7A
CYB5B
POR
SOD2
TLE3
USP13
HMOX1
FXC1
LOC696815
CWC22
IBTK
TARDBP
HECTD1
TOMM70
DPH5
DDX1
INTS4
FAM98A
CENPF
USP54
UBXN8
MRPS27
VAMP3
IRF8
TIMM10
ACSL1
MRPS9
SLU7
VPS35
GPX1
SDE2
MRPS25
PNPT1
CSNK2A2
TLE1
THTPA
LCN2
PPT1
POLK
BRD2
LOC706270
EXOSC5
NUP54
SEC24B
ENSMMUG00000007774
CTTN
VIMP
C19orf52
ACOX1
PITRM1
NUP93
MGST3
TCF12
EIF4H
TM2D3
SF3A2
XPO1
TRIP4
NUP2
TXNDC17
AP2A2
TJP1
RDX
SLC27A2
PABPC4
EXOSC2
EXOSC9
NUP133
CTNNA2
PICALM
SERPINB9
FAR2
PUS1
IL411
ZC3H7A
CAMLG
EIF1B
ACSL3
PABPC1
ELAC2
RAE1
NUP214
AP2M1
HSD17B4
DNMT1
SMU1
KIAA1468
NKX3-2
TYSND1
EIF3D
FXR1
DDX10
AKAP8L
LOC711596
AP3B1
SLC9A3R1
CNN3
AASDHPPT
CSDE1
LOC704516
UPF1
JUP
UBAP2L
MYH4
EIF1
SIRT5
EXOSC3
ATP13A3
EIF3J
DDX47
NOP14
HDAC2
GIGYF2
NUP88
AGPS
JMJD8
ZC3H13
CLCC1
NPC2
PLAT
AK3
RBM28
MAT2B
TAPT1
KIAA1033
PFDN2
TRMT1
NUP210
ENSMMUG00000029858
EIF4E2
GIPC2
SCAP
TRA2A
MPHOSPH10
SIGMAR1
ENSMMUG00000029910
PTBP2
CCDC86
LARP1
NCDN
MDN1
ENSMMUG00000029921
SERPINC1
PRUNE
MARK1
DDX21
NCL
LOC719396
PPME1
LOC695213
DCAKD
RPAP3
LARP7
MOV10
HIST1H2BJ
AAR2
LARP4B
AATF
G3BP2
IMPAD1
NINL
MYCBP2
G3BP1
IDE
SCN9A
INHBE
MEPCE
YBX2
HIST1H2BD
KLHL4
PVR
SLC3A2
LOC696428
CMSS1
HIST1H2BA
MARK3
TBC1D8B
EML5
UBOX5
LAS1L
HIST2H2BF
HS2ST1
CRTC3
CARD8
HSD17B11
ADAM9
CEP112
TMEM39B
MARK2
GGH
TENM3
GTPBP2
SCARB1
BZW2
HS6ST2
ANO6
ADAP1
BAG5
FAM162A
C1H1orf50
ZDHHC5
TMEM97
LOH12CR1
GHITM
PTGES2
RBM41
SCCPDH
GRIPAP1

Figure S5

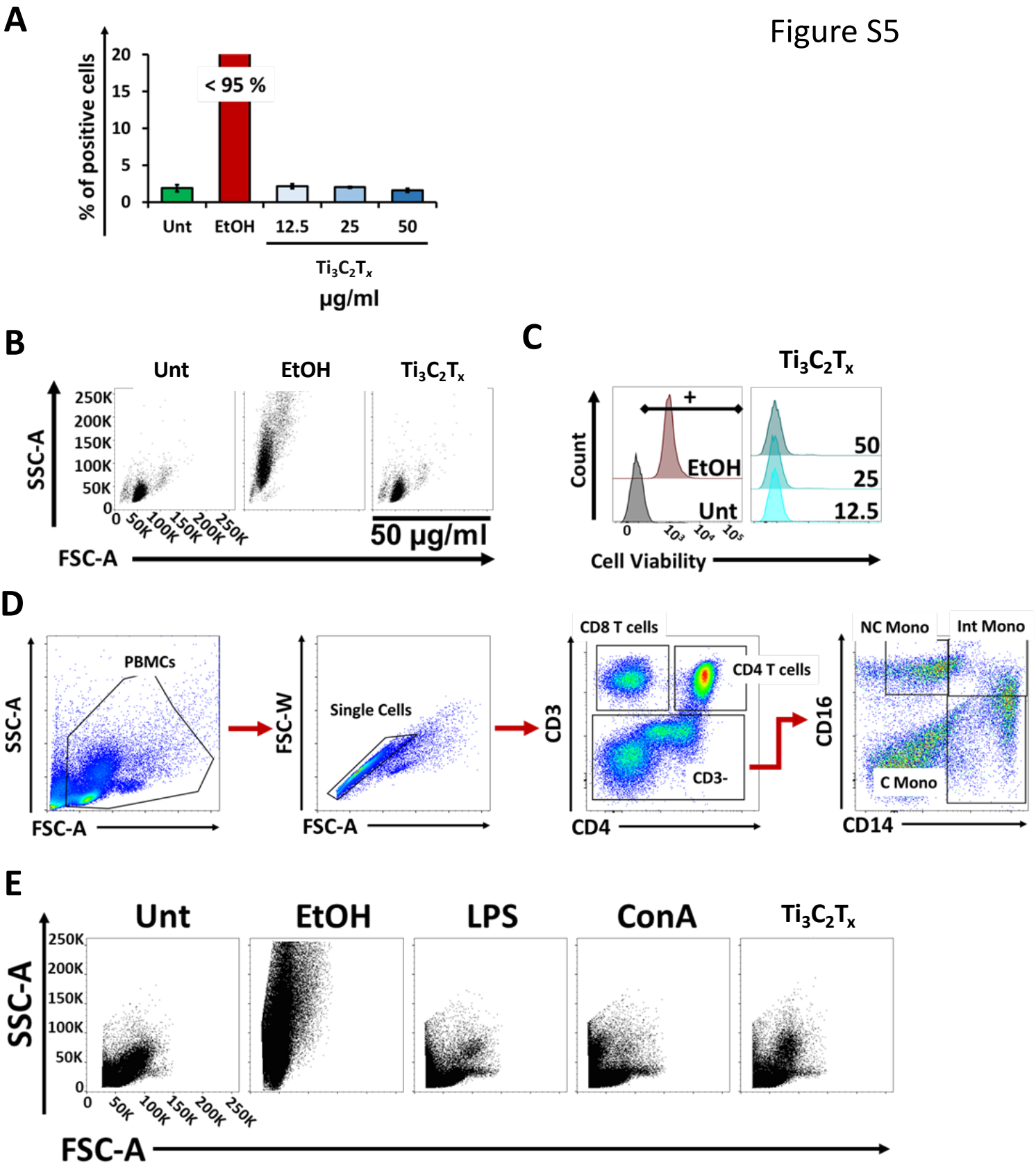
A
% of positive cells
20
15
10
5
0
< 95 %
Unt
EtOH
12.5
25
50
Ti3C2Tx
µg/ml
B
Unt
EtOH
Ti3C2Tx
SSC-A
250K
200K
150K
100K
50K
0
0 50K 100K 150K 200K 250K
50 µg/ml
FSC-A
C
Ti3C2Tx
Count
+
EtOH
Unt
50
25
12.5
0
10³ 10⁴ 10⁵
Cell Viability
D
PBMCs
SSC-A
FSC-A
Single Cells
FSC-W
FSC-A
CD8 T cells
CD4 T cells
CD3-
CD3
CD4
NC Mono
Int Mono
C Mono
CD16
CD14
E
Unt
EtOH
LPS
ConA
Ti3C2Tx
SSC-A
250K
200K
150K
100K
50K
0
0 50K 100K 150K 200K 250K
FSC-A

Figure S6

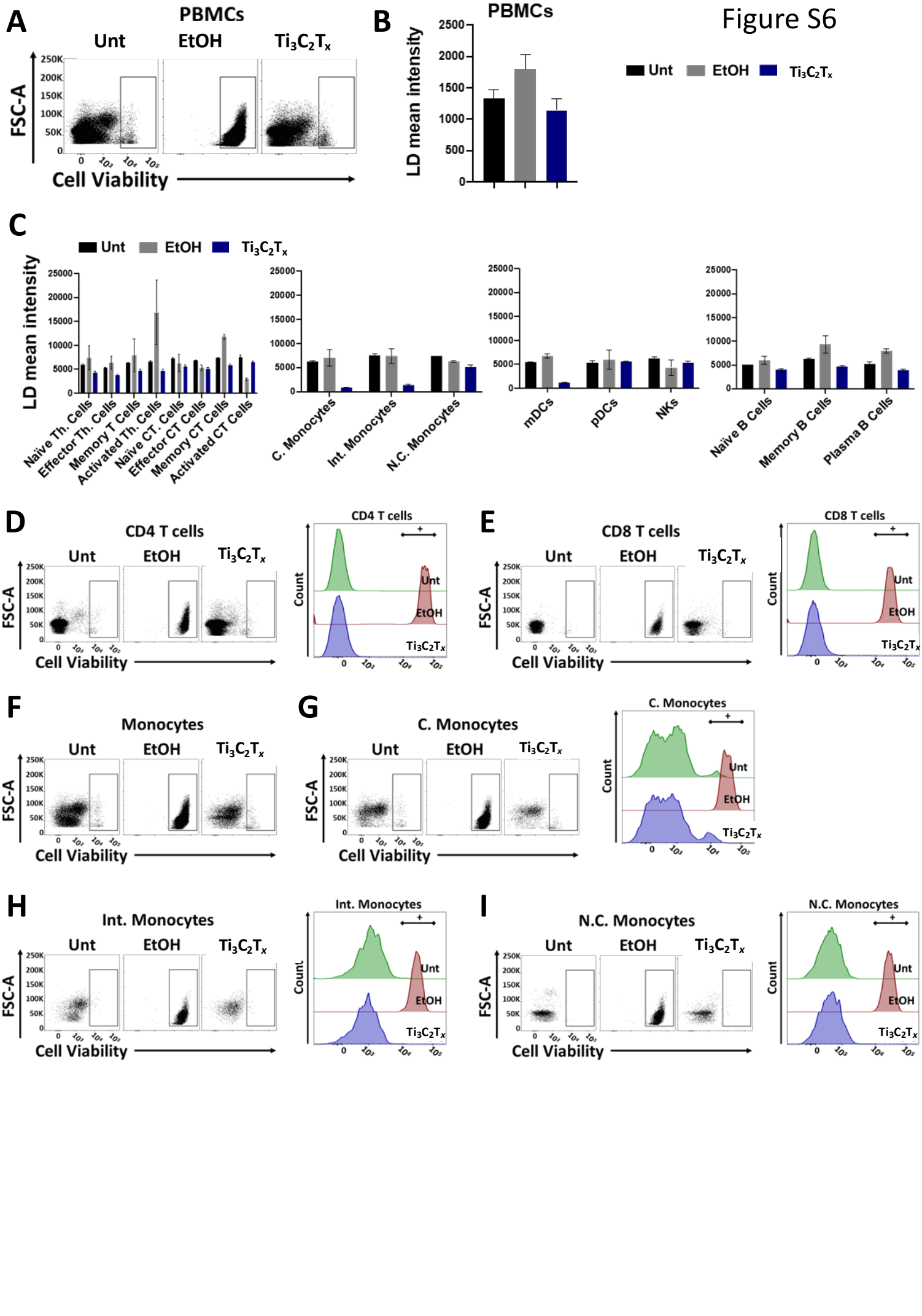
A
PBMCs
Unt
EtOH
Ti3C2Tx
FSC-A
Cell Viability
B
PBMCs
LD mean intensity
Unt
EtOH
Ti3C2Tx
C
Unt
EtOH
Ti3C2Tx
LD mean intensity
Naïve Th. Cells
Effector Th. Cells
Memory T Cells
Activated Th. Cells
Naïve CT. Cells
Effector CT Cells
Memory CT Cells
Activated CT Cells
C. Monocytes
Int. Monocytes
N.C. Monocytes
mDCs
pDCs
NKs
Naïve B Cells
Memory B Cells
Plasma B Cells
D
CD4 T cells
Unt
EtOH
Ti3C2Tx
FSC-A
Cell Viability
CD4 T cells
Count
E
CD8 T cells
CD8 T cells
F
Monocytes
G
C. Monocytes
C. Monocytes
H
Int. Monocytes
Int. Monocytes
I
N.C. Monocytes
N.C. Monocytes

Figure S7

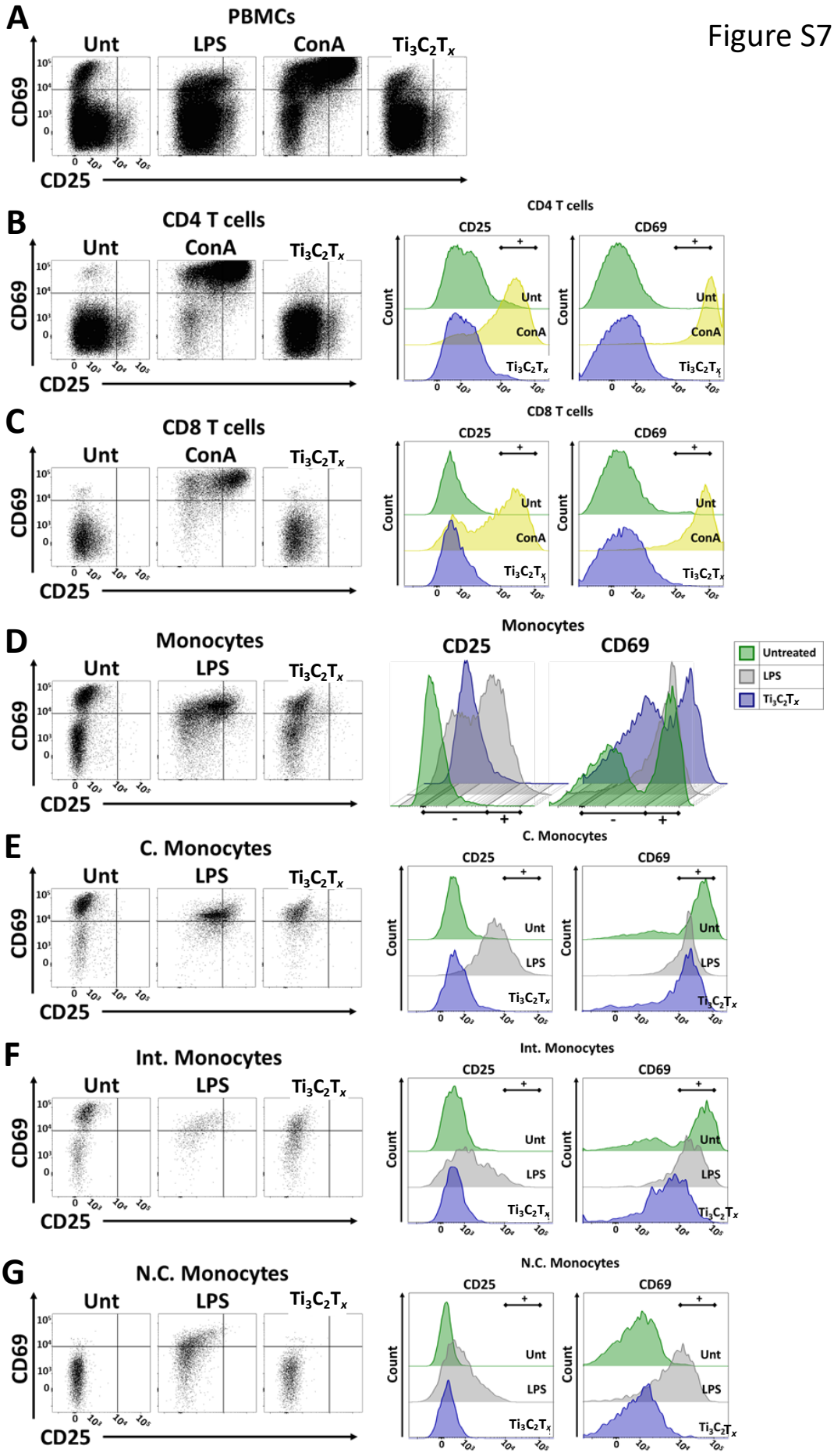
A
PBMCs
Unt
LPS
ConA
Ti3C2Tx
CD69
CD25
B
CD4 T cells
CD25
CD69
Count
Unt
ConA
C
CD8 T cells
D
Monocytes
Untreated
LPS
E
C. Monocytes
F
Int. Monocytes
G
N.C. Monocytes
H
CD25 (% of positive cells)
Ti2C3Tx
Ti2C3Tx + LPS
I
TNFα (pg/ml)

Figure S8

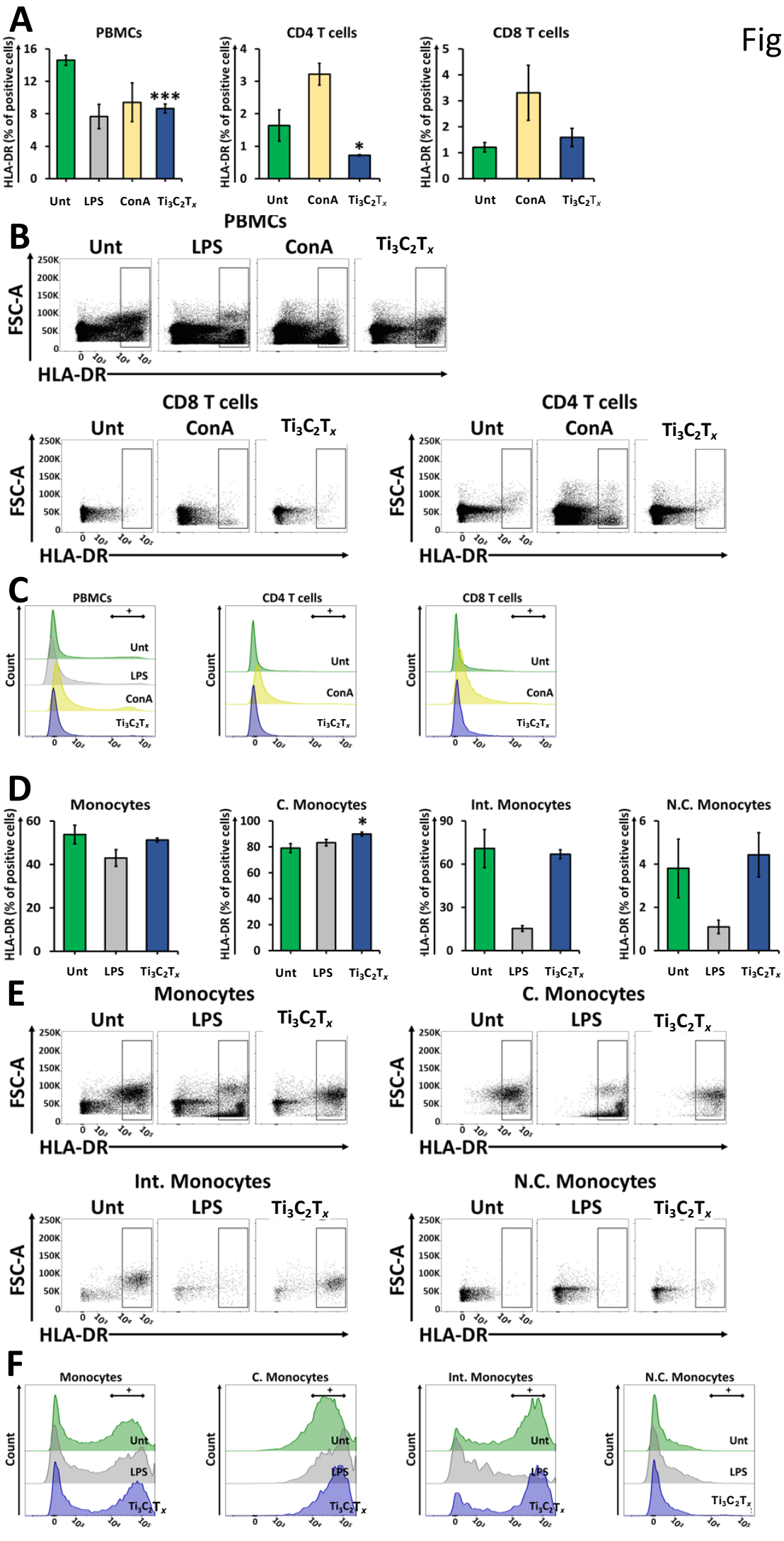
A
PBMCs
CD4 T cells
CD8 T cells
HLA-DR (% of positive cells)
Unt
LPS
ConA
Ti3C2Tx
***
*
B
PBMCs
Unt
LPS
ConA
Ti3C2Tx
FSC-A
HLA-DR
CD8 T cells
CD4 T cells
C
PBMCs
CD4 T cells
CD8 T cells
Count
D
Monocytes
C. Monocytes
Int. Monocytes
N.C. Monocytes
E
Monocytes
C. Monocytes
Int. Monocytes
N.C. Monocytes
F
Monocytes
C. Monocytes
Int. Monocytes
N.C. Monocytes

Figure S9

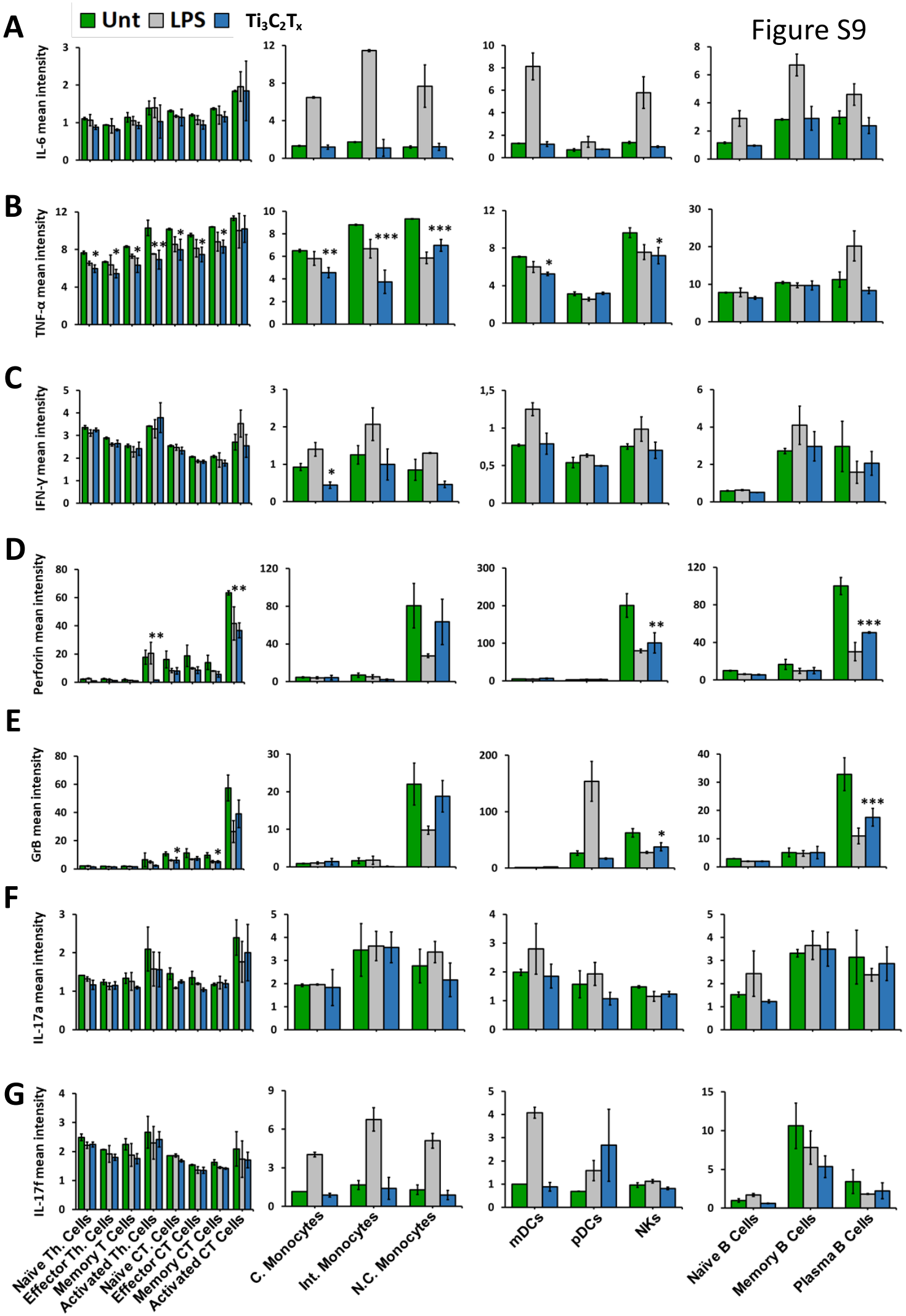
A
Unt
LPS
Ti3C2Tx
IL-6 mean intensity
B
TNF-α mean intensity
C
IFN-γ mean intensity
D
Perforin mean intensity
E
GrB mean intensity
F
IL-17a mean intensity
G
IL-17f mean intensity
Naïve Th. Cells
Effector Th. Cells
Memory T Cells
Activated Th. Cells
Naïve CT. Cells
Effector CT Cells
Memory CT Cells
Activated CT Cells
C. Monocytes
Int. Monocytes
N.C. Monocytes
mDCs
pDCs
NKs
Naïve B Cells
Memory B Cells
Plasma B Cells

Figure S10

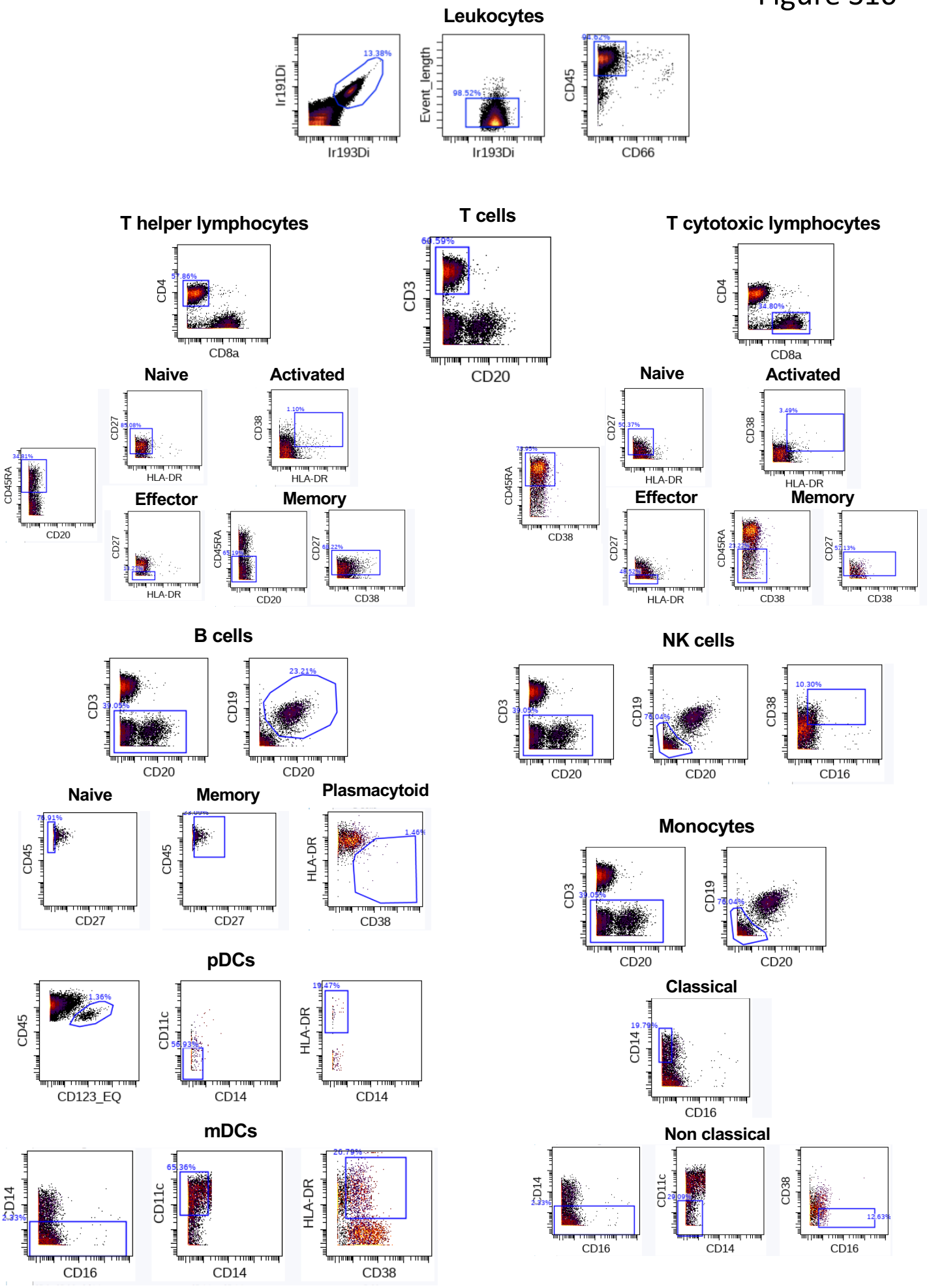
Leukocytes
Ir191Di
Ir193Di
13.38%
Event_length
Ir193Di
98.52%
CD45
CD66
T helper lymphocytes
CD4
CD8a
T cells
CD3
CD20
60.59%
T cytotoxic lymphocytes
CD4
CD8a
34.80%
Naive
Activated
CD27
HLA-DR
CD38
1.10%
CD45RA
CD20
Effector
Memory
CD27
HLA-DR
CD45RA
CD20
CD27
CD38
Naive
Activated
CD27
HLA-DR
CD38
3.49%
CD45RA
CD38
Effector
Memory
CD27
HLA-DR
CD45RA
CD38
CD27
CD38
B cells
CD3
CD20
CD19
CD20
23.21%
NK cells
CD3
CD20
CD19
CD20
CD38
CD16
10.30%
Naive
Memory
Plasmacytoid
CD45
CD27
CD45
CD27
HLA-DR
CD38
1.46%
Monocytes
CD3
CD20
CD19
CD20
pDCs
CD45
CD123_EQ
1.36%
CD11c
CD14
HLA-DR
CD14
19.47%
Classical
CD14
CD16
19.79%
mDCs
CD14
CD16
CD11c
CD14
65.36%
HLA-DR
CD38
26.79%
Non classical
CD14
CD16
CD11c
CD14
CD38
CD16
12.63%